物 理 化 学 学 报

Acta Phys. -Chim. Sin. **2024,** *40* (4), 2305026 (1 of 6)

[Article] doi: 10.3866/PKU.WHXB202305026 www.whxb.pku.edu.cn

Metal-Organic Framework-Derived Nickel Nanoparticles for Efficient CO_2 Electroreduction in Wide Potential Windows

Bizhu Shao [1,†], Huijun Dong [1,†], Yunnan Gong [1,*], Jianhua Mei [1], Fengshi Cai [1], Jinbiao Liu [2,*], Dichang Zhong [1,*], Tongbu Lu [1]

[1] Institute for New Energy Materials and Low Carbon Technologies, School of Materials Science and Engineering, Tianjin University of Technology, Tianjin 300384, China.

[2] School of Chemistry and Chemical Engineering, Tianjin University of Technology, Tianjin 300384, China.

Abstract: The electrocatalytic carbon dioxide (CO_2) reduction has gained recognition as an outstanding approach for transforming CO_2 into renewable energy products. To accomplish this reduction reaction, the development of efficient electrocatalysts is required. Nickel-based electrocatalysts have been extensively investigated for CO_2 reduction; however, nickel nanoparticles (Ni_{NPs}) have demonstrated limited catalytic performance. In this study, Ni_{NPs} implanted in N-doped porous carbon (Ni_{NPs}-NC) were prepared by thermal treatment of nickel metal-organic framework, urea, and carbon black under an N_2 atmosphere. The Ni_{NPs}-NC exhibited high catalytic performance for the electroreduction of CO_2 to CO in both H-type and flow cells. In the H-type cell, the CO faradaic efficiencies (FEs) of Ni_{NPs}-NC exceeded 90% in the potential window from −0.67 to −1.07 V *vs.* reversible hydrogen electrode (RHE), reaching a maximum CO FE of approximately 100% at −0.87 V *vs.* RHE. In the flow cell, the CO selectivities of Ni_{NPs}-NC exceeded 95% in the potential window from −0.50 to −0.70 V *vs.* RHE. The fast charge transfer, as demonstrated by electrochemical impedance spectroscopy and Tafel slope, can be attributed to the high catalytic activity of Ni_{NPs}-NC. This study provides a simple method to develop highly efficient catalysts for electrocatalytic CO_2 reduction.

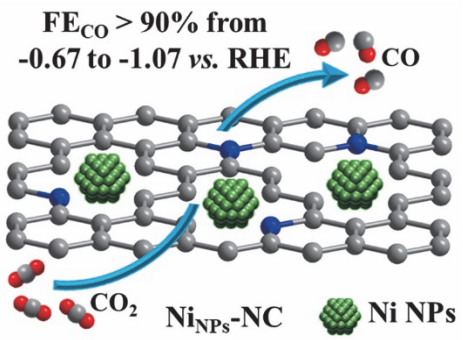

Key Words: Nickel nanoparticle; Electrocatalyst; CO_2 reduction; Metal-organic framework; Thermal treatment

金属有机框架衍生镍纳米颗粒在宽电位窗口内高效电催化二氧化碳还原

邵碧珠[1,†]，董慧君[1,†]，龚云南[1,*]，梅剑华[1]，蔡锋石[1]，刘金彪[2,*]，钟地长[1,*]，鲁统部[1]

[1] 天津理工大学新能源材料与低碳技术研究院，材料科学与工程学院，天津 300384

[2] 天津理工大学化学化工学院，天津 300384

摘要：电催化二氧化碳(CO_2)还原被认为是将CO_2转化为可再生能源产品的一种有前途的方法。开发性能优异的电催化剂高效完成这一重要反应是关键。镍基催化剂广泛应用于电催化CO_2还原研究，但是，镍纳米颗粒经常表现较差的催化性能。在本文中，通过在氮气气氛中高温热解镍基金属有机骨架(MOF)、尿素和炭黑混合物，获得了镍纳米颗粒负载于

Received: May 12, 2023; Revised: June 8, 2023; Accepted: June 8, 2023; Published online: June 16, 2023.

† These authors contributed to this work equally.

*Corresponding authors. Emails: yngong@email.tjut.edu.cn (Y.G.); liujinbiao007@126.com (J.L.); dczhong@email.tjut.edu.cn (D.Z.)

The project was supported by the National Key R&D Program of China (2022YFA1502902), National Natural Science Foundation of China (22271218, 22071182, 22001043, 21931007), and Natural Science Foundation of Tianjin City (20JCYBJC00380).

国家重点研发计划(2022YFA1502902), 国家自然科学基金(22271218, 22071182, 22001043, 21931007), 天津市自然科学基金(20JCYBJC00380)资助项目

多孔碳氮中的催化材料(Ni_{NPs}-NC)。有趣的是，Ni_{NPs}-NC在H型和流动相电池中都表现出优异的CO_2电还原性能。在H型电解池和−0.67 – −1.07 V *vs.* RHE (可逆氢电极)电位窗口内，Ni_{NPs}-NC催化CO_2还原为CO的法拉第效率大于90%，其中，在−0.87 V *vs.* RHE时，CO的法拉第效率约为100%。在流动相电解池和−0.50 – −0.70 V *vs.* RHE电位窗口内，Ni_{NPs}-NC催化CO_2还原为CO的选择性大于95%。电化学阻抗谱图和塔菲尔斜率表征显示，Ni_{NPs}-NC的高催化活性归因于其在催化过程中的快速电荷转移。本文提供了一种制备高效CO_2电还原催化剂的方法。

关键词：镍纳米颗粒；电催化剂；二氧化碳还原；金属有机框架；热处理
中图分类号：O643

1 Introduction

The large-scale combustion of fossil fuels has resulted in excessive emission of carbon dioxide (CO_2), which has caused serious environmental problems [1,2]. In the past decades, some technologies have been developed to alleviate the excessive emission of CO_2 [3,4]. Among them, electrocatalytic CO_2 reduction has been considered as a promising method for lowering CO_2 accumulation and converting it into value-added products such CO, HCOOH, CH_4 and C_2H_4, *etc.* [5–7]. However, owing to the high stability of the CO_2 molecule, as well as the competing hydrogen evolution reaction (HER), this CO_2 conversion technology often displays low activity and selectivity [8–11]. In consequence, developing efficient electrocatalysts to reduce CO_2 with high performance and selectivity is urgently demanded.

Metal-organic frameworks (MOFs), as the new crystalline porous materials, are fabricated by metal ions/clusters and organic ligands, which not only show great potentials for various applications, but also are promising candidates to produce desired materials for catalysis [12–18]. Recently, MOFs have been demonstrated to be ideal platforms to construct single-atom catalysts (SACs) for electrocatalytic CO_2 reduction [19–25]. Particularly, the MOF-derived single-atom nickel electrocatalysts usually show high performance for the reduction of CO_2 to CO [26–35]. Nevertheless, they tend to agglomerate to form nanoparticles (NPs) in the synthetic process because of the high surface energy, which often show lowered catalytic performance over pure SACs [23,29]. Therefore, the construction of MOF-derived Ni NPs for electrocatalytic CO_2 reduction with high activity and selectivity is highly desired yet remains a grand challenge.

Herein, we prepared Ni NPs implanted in N-doped porous carbon (Ni_{NPs}-NC) by the calcination of nickel-based MOF (Ni-MOF), urea and carbon black under N_2 atmosphere for electrocatalytic CO_2 reduction (Scheme 1). The catalytic results demonstrate that Ni_{NPs}-NC exhibits excellent performance for electrocatalytic CO_2 reduction, with CO faradaic efficiencies (FEs) of exceeded 90% from −0.67 to −1.07 V *vs.* reversible hydrogen electrode (RHE) in the H-type cell. The maximum CO FE is ~100% at −0.87 V *vs.* RHE. Furthermore, in the flow cell, Ni_{NPs}-NC also shows high CO selectivities of exceeded 95% from −0.50 to −0.70 V *vs.* RHE. The results of electrochemical impedance spectroscopy and Tafel slope unveil that the high performance of Ni_{NPs}-NC could be attributed to its fast charge-transfer.

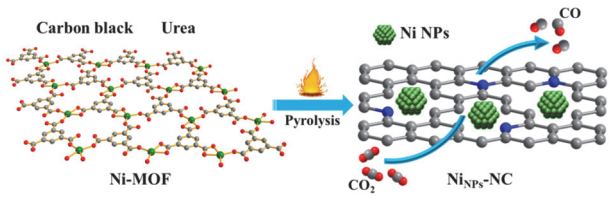

Scheme 1 Illustration showing the construction of Ni_{NPs}-NC catalyst for electrocatalytic CO_2 reduction to CO.

2 Experimental section

2.1 Preparation of Ni-MOF

Ni-MOF was prepared based on literature methods [36]. 145 mg $Ni(NO_3)_2{\cdot}6H_2O$ (99.99%, 0.5 mmol), 105 mg 1,3,5-benzenetricarboxylic acid (H_3BTC, 98%, 0.5 mmol) and 10 mL *N*,*N*-dimethylformamide (DMF, 99.5%) were added in the Teflon-lined stainless steel reactor, which was heated at 130 °C for 3 d. Yellow-green block crystals of Ni-MOF were obtained by filtration and washed with DMF. Yield: 55%.

2.2 Preparation of Ni_{NPs}-NC and NC

A mixture of 40 mg Ni-MOF, 2 g urea (99%) and 20 mg carbon black (99.9%) was ball-milled for 10 h continuously (XQM-0.4A, Changsha Tianchuang Powder Technology Company Limited, China). Then, the mixture was heated in N_2 atmosphere at 520 and 800 °C for 1 h, respectively. Black powder of Ni_{NPs}-NC was obtained. The synthetic procedure of NC is similar to that of Ni_{NPs}-NC, except for the absence of Ni-MOF.

2.3 Characterization

Powder X-ray diffraction (XRD) measurements were carried out using a smart X-ray diffractometer (SmartLab 9 kW, Rigaku, Japan). N_2 sorption measurements were performed at 77 K using a gas adsorption analyzer (BELSORP-Mas, Microtrac BEL, Japan). The content of Ni was quantified by an inductively coupled plasma mass spectrometer (ICP-MS, iCAP RQ, Germany). The ^{1}H NMR spectroscopy was conducted on 400 MHz spectrometer (AVANCE III HD, Bruker, Germany). Electrochemical impedance spectroscopy (EIS) measurements were conducted on an electrochemical workstation (CHI660E, Shanghai Chenhua, China). The gas products for CO_2

electroreduction were analyzed by gas chromatography (GC-2014 + ATF, 230C, Shimadzu, Japan). The isotopes of ^{13}C for CO was analyzed using mass spectrometry (7890B/5977B, Agilent, USA).

2.4 Electrochemical measurements

Electrochemical measurements were performed in both H-type and flow cells using an electrochemical station (CHI760E). In the H-type cell, the Nafion 117 membrane (Dupont, USA) was used as proton exchange membrane. Each compartment contains 17 mL 0.5 mol·L^{-1} $KHCO_3$ (99%) electrolyte. Flow cell was fabricated with a CO_2 gas compartment and two liquid compartments with channels. CO_2 and electrolyte (97%, 1.0 mol·L^{-1} KOH) were separated by gas diffusion electrodes (GDEs). Ag/AgCl (saturated KCl) and Pt foil were used as reference and counter electrodes, respectively. All potentials were converted to RHE. In the H-type cell, 2.5 mg catalyst was first dispersed in the mixture of C_2H_5OH (99.5%, 360 μL), H_2O (120 mL) and Nafion solution (20 μL) to prepare catalyst ink. Then, the homogeneous ink (100 μL) was loaded onto a carbon cloth (2 cm × 0.5 cm). In the flow cell, the catalyst ink was prepared by dispersing catalyst (4.0 mg) in the mixture of ethanol (480 μL) and Nafion solution (20 μL). The mixture was then loaded onto a carbon paper (2 cm × 2 cm). A CO_2-saturated electrolyte was prepared by purging CO_2 gas into liquid electrolyte for 30 min.

3 Results and discussion

3.1 Characterization

Powder XRD pattern of the synthesized Ni-MOF is basically identical with the simulated one, demonstrating the high purity of Ni-MOF (Fig. S1, Supporting Information). Afterward, the calcination of Ni-MOF, urea and carbon black in N_2 atmosphere was performed to generate nickel nanoparticles implanted in N-doped porous carbon (Ni_{NPs}-NC). Powder XRD pattern confirms the formation of Ni NPs, in which the 44.5°, 51.7° and 76.2° peaks are assigned to the (111), (200) and (220) diffractions, respectively (Fig. 1a). N_2 adsorption measurement of Ni_{NPs}-NC at 77 K and 101325 Pa reveals a reversible type II isotherm. The Brunauer-Emmett-Teller (BET) surface area of Ni_{NPs}-NC is 189.8 m^2·g^{-1} and the pore size distribution of Ni_{NPs}-NC is 0.7 to 5.3 nm (Figs. 1b and S2). The result of CO_2 adsorption isotherm demonstrates that the adsorption capacity of Ni_{NPs}-NC is 9.0 cm^3·g^{-1} at 298 K and 101325 Pa (Fig. S3). Moreover, the content of Ni in Ni_{NPs}-NC is 13.8% (mass fraction) determined by ICP-MS. In addition, the N-doped porous carbon (NC) was synthesized by the pyrolysis of urea and carbon black in N_2 atmosphere. Powder XRD pattern of NC shows two broad peaks located at 20°–30° and 40°–45° respectively, which correspond to the (002) and (101) crystal faces of carbon black (C) (Fig. 1a). N_2 adsorption measurements of NC and C at 77 K and 101325 Pa also unveil reversible type II isotherms with the BET surface areas of 186.2 and 218.5 m^2·g^{-1}, respectively. Their pore size distributions are 0.6–4.8 nm and 0.5–4.4 nm, respectively (Figs. 1b, S4 and S5). CO_2 adsorption measurements at 101325 Pa and 298 K show that the CO_2 uptakes of NC and C are 9.5 and 11.9 cm^3·g^{-1}, respectively (Figs. S6 and S7).

3.2 Electrocatalytic CO_2 reduction

Electrocatalytic reduction of CO_2 for C, NC and Ni_{NPs}-NC were carried out in both H-type and flow cells. The linear sweep voltammetry (LSV) measurements show that the current densities of them in CO_2-saturated electrolyte are higher than those of in Ar atmosphere in the H-type cell, demonstrating their catalytic activities for electrocatalytic CO_2 reduction (Figs. S8–S10). As shown in Fig. 2a, Ni_{NPs}-NC exhibits a higher current density than C and NC in CO_2 atmosphere, manifesting the best performance of Ni_{NPs}-NC for CO_2 electroreduction among all three catalysts. Moreover, the CO FEs of C, NC and Ni_{NPs}-NC for electrocatalytic CO_2 reduction were examined from −0.57 to −1.17 V *vs.* RHE. Impressively, the Ni_{NPs}-NC shows high CO FEs of exceeded 90% from −0.67 to −1.07 V *vs.* RHE. At −0.87 V *vs.* RHE, the CO FE reaches maximum value of about 100% (Fig. 2b). Meanwhile, Ni_{NPs}-NC achieves a large CO partial current density (J_{CO}) of 23.72 mA·cm^{-2} at −0.97 V *vs.* RHE (Fig. 2c). The CO FEs and J_{CO} of Ni_{NPs}-NC are larger than those of C and NC in all tested potentials (Fig. 2c), suggesting that the implantation of Ni NPs in N-doped porous carbon significantly enhances electrocatalytic performance for the reduction of CO_2 to CO. Apart from the excellent activity and selectivity, Ni_{NPs}-NC also

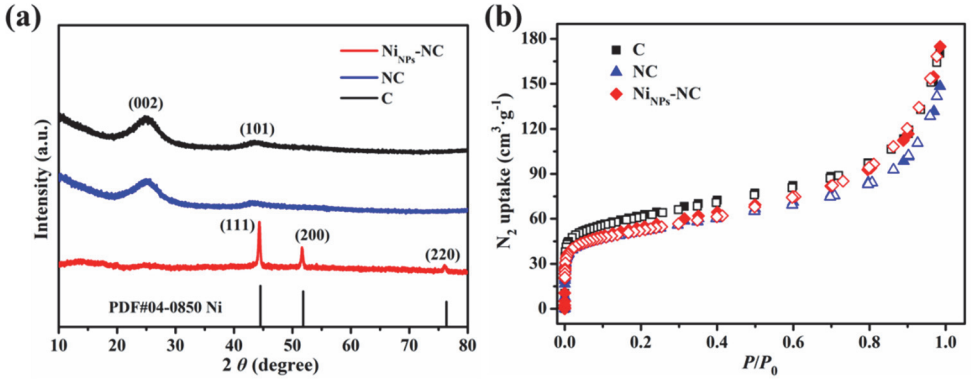

Fig. 1 (a) Powder XRD patterns for Ni_{NPs}-NC, NC and C. (b) N_2 adsorption isotherms for Ni_{NPs}-NC, NC and C.

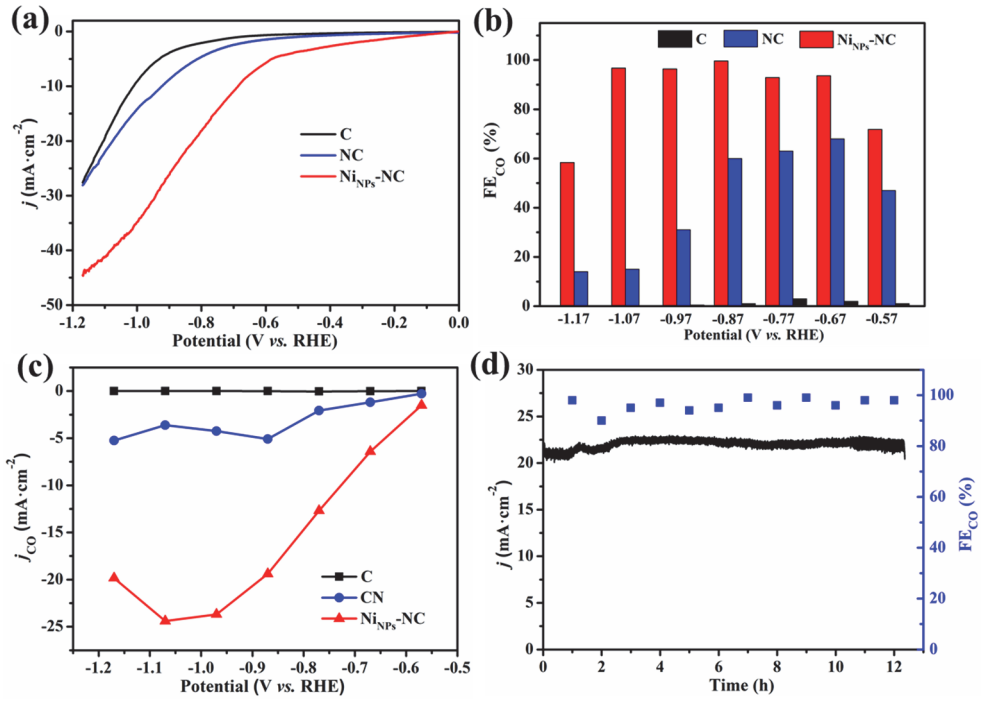

Fig. 2 (a) LSV curves of C, NC and Ni$_{NPs}$-NC in the CO_2-saturated electrolyte. (b) CO FEs of C, NC and Ni$_{NPs}$-NC. (c) The J_{CO} of C, NC and Ni$_{NPs}$-NC. (d) The stability measurement for Ni$_{NPs}$-NC at −0.87 V *vs.* RHE.

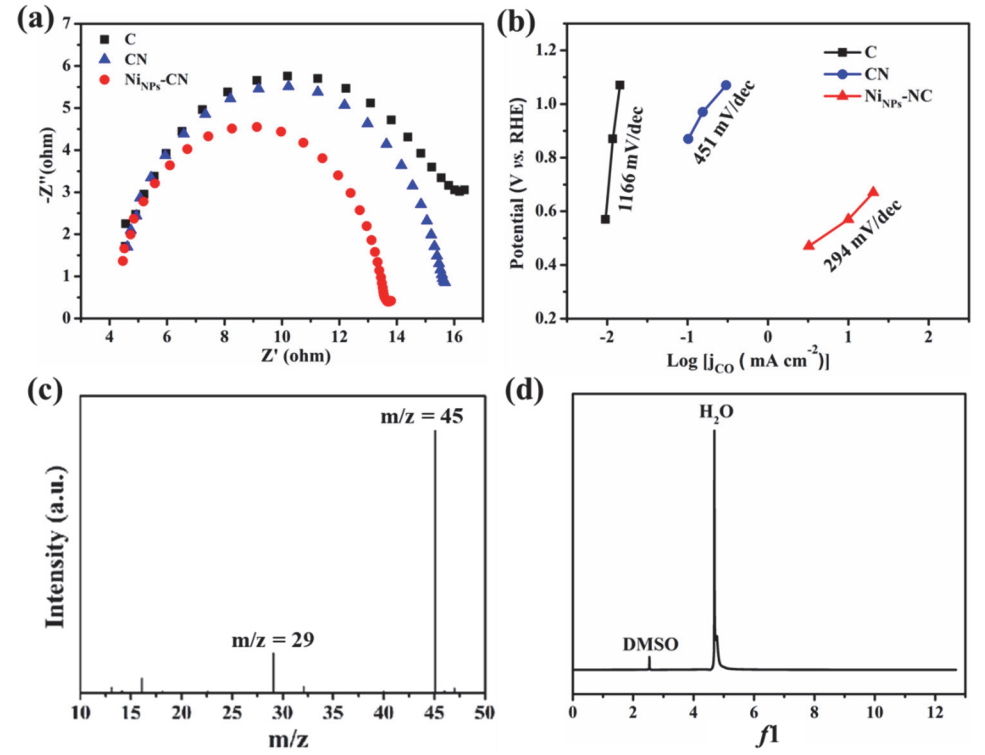

Fig. 3 (a) EIS plots of C, NC and Ni$_{NPs}$-NC. (b) Tafel plots of C, NC and Ni$_{NPs}$-NC. (c) MS of the gaseous products for electrocatalytic $^{13}CO_2$ reduction over Ni$_{NPs}$-NC. (d) ^{1}H NMR spectrum of the electrolyte after 30 min electrolysis at −0.87 V *vs.* RHE over Ni$_{NPs}$-NC.

exhibits good catalytic stability for CO_2 electroreduction in the H-type cell. The current density and FE for CO production are nearly unchanged after electrolyzation for 12 h at −0.87 V *vs.* RHE (Fig. 2d).

In order to clarify the higher activity of Ni$_{NPs}$-NC than C and NC, EIS and Tafel slopes were conducted. The results of EIS demonstrate that Ni$_{NPs}$-NC shows the smallest semicircle radius, suggesting the lowest charge-transfer resistance of Ni$_{NPs}$-NC among the tested electrocatalysts (Fig. 3a). The Tafel slope of Ni$_{NPs}$-NC is calculated to be 294 mV·dec^{-1}, which is

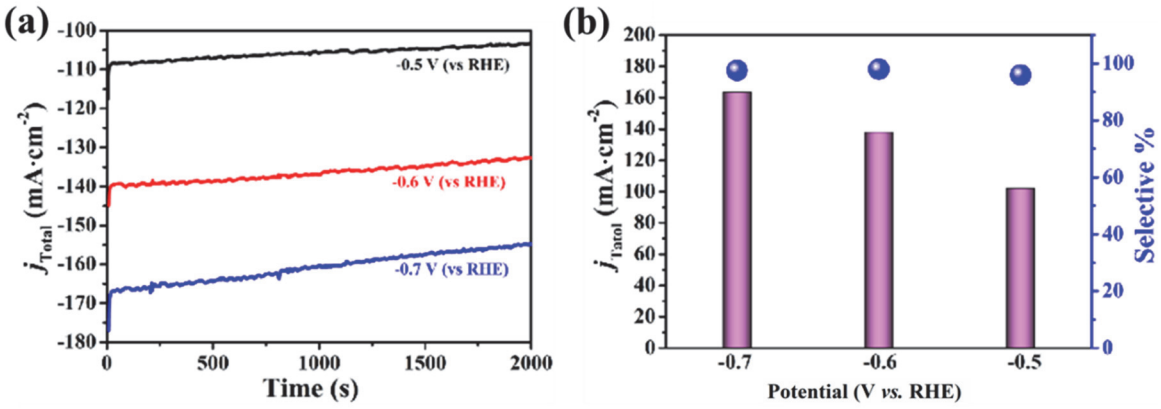

Fig. 4 (a) The current density of Ni_{NPs}-NC during long-time electrolysis at different potentials. (b) The current density and CO selectivities of Ni_{NPs}-NC at different potentials.

smaller than C (1166 mV·dec^{-1}) and NC (451 mV·dec^{-1}), implying the favorable kinetics of Ni_{NPs}-NC for the formation of CO (Fig. 3b). These results indicate that Ni_{NPs}-NC exhibits the fastest charge-transfer and thus the highest catalytic performance for the electroreduction of CO_2 to CO among all three catalysts. To confirm the carbon source of CO, the $^{13}CO_2$ isotope trace experiment of Ni_{NPs}-NC was performed. The result of mass spectrum (MS) exhibits a signal peak at m/z = 29, which is attributed to ^{13}CO, confirming that the CO indeed comes from CO_2 reduction. Furthermore, no liquid products are detected over Ni_{NPs}-NC by ^1H NMR spectroscopy, further affirming the high selectivity of CO (Fig. 3d).

To further investigate catalytic performance of Ni_{NPs}-NC, the electrocatalytic CO_2 reduction was carried out in the flow cell. LSV measurement shows that Ni_{NPs}-NC exhibits large current density in CO_2-saturated 1.0 mol·L^{-1} KOH (Fig. S11). At −0.50, −0.60 and −0.70 V *vs.* RHE, the current densities of Ni_{NPs}-NC are about 163, 138 and 102 mA·cm^{-2}, respectively, and the CO selectivities of Ni_{NPs}-NC exceed 95% in these potentials (Fig. 4). These results clearly demonstrate exceptionally catalytic performance of MOF-derived Ni NPs for the electroreduction of CO_2 to CO.

4 Conclusions

In summary, Ni NPs implanted in N-doped porous carbon (Ni_{NPs}-NC) has been prepared by the pyrolysis of nickel-based MOF, urea and carbon black. The results of electrocatalytic CO_2 reduction demonstrate that Ni_{NPs}-NC shows high performance for the production of CO in both H-type and flow cells. In the H-type cell, the CO FEs of Ni_{NPs}-NC exceed 90% from −0.67 to −1.07 *vs.* RHE, with the maximum CO FE of ~100% at −0.87 V *vs.* RHE. Moreover, the CO selectivities of Ni_{NPs}-NC exceed 95% from −0.50 to −0.70 *vs.* RHE in the flow cell. The electrochemical impedance spectroscopy and Tafel slope disclose that Ni_{NPs}-NC exhibits fast charge-transfer and thus accounting for its excellent catalytic performance. This work develops efficient metal nanoparticles for electrocatalytic CO_2 reduction.

Author Contributions: Conceptualization, Y.G. and D.Z.; Methodology, B.S. H.D. F.C. and J.L.; Formal Analysis, J.M.; Writing-Original Draft Preparation, B.S. and Y.G.; Writing-Review & Editing, D.Z.; Supervision, D.Z. and T.L.; Funding Acquisition, Y.G., D.Z. and T.L.

Supporting Information: Powder XRD pattern, pore diameter distributions, CO_2 adsorption isotherms, LSV curves.

Notes: The authors declare no competing financial interest.

References

(1) Dowell, N. M.; Fennell, P. S.; Shah, N.; Maitland, G. C. *Nat. Clim. Change* **2017,** *7*, 243. doi: 10.1038/NCLIMATE3231

(2) Shakun, J. D.; Clark, P. U.; He, F.; Marcott, S. A.; Mix, A. C.; Liu, Z.; Otto-Bliesner, B.; Schmittner, A.; Bard, E. *Nature* **2012,** *484*, 49. doi: 10.1038/nature10915

(3) Ding, M. L.; Flaig, R. W.; Jiang, H.-L.; Yaghi, O. M. *Chem. Soc. Rev.* **2019,** *48*, 2783. doi: 10.1039/c8cs00829a

(4) Wu, Q.-J.; Liang, J.; Huang, Y.-B.; Cao, R. *Chem. Res.* **2022,** *55*, 2978. doi: 10.1021/acs.accounts.2c00326

(5) Wang, C. L.; Lv, Z. H.; Yang, W. X.; Feng, X.; Wang, B. *Chem. Soc. Rev.* **2023,** *52*, 1382. doi: 10.1039/d2cs00843b

(6) Lv, F.; Han, N.; Qiu, Y.; Liu, X. J.; Luo, J.; Li, Y. G. *Coord. Chem. Rev.* **2020,** *422*, 213435. doi: 10.1016/j.ccr.2020.213435

(7) Wu, Y. S.; Jiang, Z.; Lu, X.; Liang, Y. Y.; Wang, H. H. *Nature* **2019,** *575*, 639. doi: 10.1038/s41586-019-1760-8

(8) Li, L.; Li, X. D.; Sun, Y. F.; Xie, Y. *Chem. Soc. Rev.* **2022,** *51*, 1234. doi: 10.1039/d1cs00893e

(9) Xie, W.; Li, H.; Cui, G.; Li, J.; Song, Y.; Li, S.; Zhang, X.; Lee, J. Y.; Shao, M.; Wei, M. *Angew. Chem. Int. Ed.* **2021,** *60*, 7382. doi: 10.1002/ange.202014655

(10) Zhang, N.; Zheng, F. F.; Huang, B. L.; Ji, Y. J.; Shao, Q.; Li, Y. Y.; Xiao, X. H.; Huang, X. Q. *Adv. Mater.* **2020,** *32*, 1906477.

doi: 10.1002/adma.201906477

(11) Du, Y. D.; Meng, X. T.; Wang, Z.; Zhao, X.; Qiu, J. S. *Acta Phys. -Chim. Sin*. **2022,** *38*, 2101009. [杜亚东, 孟祥桐, 汪珍, 赵鑫, 邱介山. 物理化学学报, **2022,** *38*, 2101009.] doi: 10.3866/PKU.WHXB202101009

(12) Gong, W.; Chen, Z. J.; Dong, J. Q.; Liu, Y.; Cui, Y. *Chem. Rev*. **2022,** *122*, 9078. doi: 10.1021/acs.chemrev.1c00740

(13) Zhao, M. T.; Huang, Y.; Peng, Y. W.; Huang, Z. Q.; Ma, Q. L.; Zhang, H. *Chem. Soc. Rev*. **2018,** *47*, 6267. doi: 10.1039/c8cs00268a

(14) Du, J.; Li, F.; Sun, L. C. *Chem. Soc. Rev.* **2021,** *50*, 2663. doi: 10.1039/d0cs01191f

(15) Gao, Z. Q.; Wang, C. Y.; Li, J. J.; Zhu, Y. T.; Zhang, Z. C.; Hu, W. P. *Acta Phys. -Chim. Sin*. **2021,** *37*, 2010025. [高增强, 王聪勇, 李俊俊, 朱亚廷, 张志成, 胡文平. 物理化学学报, **2021,** *37*, 2010025.] doi: 10.3866/PKU.WHXB202010025

(16) Zou, L. L.; Hou, C.-C.; Liu, Z.; Pang, H.; Xu, Q. *J. Am. Chem. Soc*. **2018,** *140*, 15393. doi: 10.1021/jacs.8b09092

(17) Shen, Y.; Pan, T.; Wang, L.; Ren, Z.; Zhang, W. N.; Huo, F. W. *Adv. Mater*. **2021,** *33*, 2007442. doi: 10.1002/adma.202007442

(18) Bigdeli, F.; Lollar, C. T.; Morsali, A.; Zhou, H.-C. *Angew. Chem. Int. Ed*. **2020,** *59*, 4652. doi: 10.1002/anie.201900666

(19) Jiao, L.; Zhang, R.; Wan, G.; Yang, W. J.; Wan, X.; Zhou, H.; Shui, J. L.; Yu, S.-H.; Jiang, H.-L. *Nat. Commun*. **2020,** *11*, 2831. doi: 10.1038/s41467-020-16715-6

(20) Wang, X. Q.; Chen, Z.; Zhao, X. Y.; Yao, T.; Chen, W. X.; You, R.; Zhao, C. M.; Wu, G.; Wang, J.; Huang, W. X.; *et al*. *Angew. Chem. Int. Ed*. **2018,** *57*, 1944. doi: 10.1002/anie.201712451

(21) Zhang, E. H.; Wang, T.; Yu, K.; Liu, J.; Chen, W. X.; Li, A.; Rong, H. P.; Lin, R.; Ji, S. F.; Zheng, X. S.; *et al*. *J. Am. Chem. Soc*. **2019,** *141*, 16569. doi: 10.1021/jacs.9b08259

(22) Huang, H. G.; Shen, K.; Chen, F. F.; Li, Y. W. *ACS Catal*. **2020,** *10*, 6579. doi: 10.1021/acscatal.0c01459

(23) Jiao, L.; Jiang, H.-L. *Chem* **2019,** *5*, 786. doi: 10.1016/j.chempr.2018.12.011

(24) Ye, J. Q.; Yan, J. P.; Peng, Y. L.; Li, F. W.; Sun, J. *Catal. Today* **2023,** *410*, 68. doi: 10.1016/j.cattod.2022.09.005

(25) Cheng, H. Y.; Wu, X. M.; Feng, M. M.; Li, X. C.; Lei, G. P.; Fan, Z. H.; Pan, D. W.; Cui, F. J.; He. G. H. *ACS Catal*. **2021,** *11*, 12673. doi: 10.1021/acscatal.1c02319

(26) Yan, C. C.; Li, H. B.; Ye, Y. F.; Wu, H. H.; Cai, F.; Si, R.; Xiao, J. P.; Miao, S.; Xie, S. H.; Yang, F.; *et al*. *Energy Environ. Sci.* **2018,** *11*, 1204. doi: 10.1039/c8ee00133b

(27) Zhang, Y.; Jiao, L.; Yang, W. J.; Xie, C. F.; Jiang, H.-L. *Angew. Chem. Int. Ed.* **2021,** *60*, 7607. doi: 10.1002/anie.202016219

(28) Zhao, C. M.; Dai, X. Y.; Yao, T.; Chen, W. X.; Wang, X. Q.; Wang, J.; Yang, J.; Wei, S. Q.; Wu, Y. E.; Li, Y. D. *J. Am. Chem. Soc*. **2017,** *139*, 8078. doi: 10.1021/jacs.7b02736

(29) Gong, Y.-N.; Jiao, L.; Qian, Y. Y.; Pan, C.-Y.; Zheng, L. R.; Cai, X. C.; Liu, B.; Yu, S.-H.; Jiang, H.-L. *Angew. Chem. Int. Ed*. **2020,** *59*, 2705. doi: 10.1002/anie.201914977

(30) Lu, P. L.; Yang, Y. J.; Yao, J. N.; Wang, M.; Dipazir, S.; Yuan, M. L.; Zhang, J. X.; Wang, X.; Xie, Z. J.; Zhang, G. J. *Appl. Catal. B* **2019,** *241*, 113. doi: 10.1016/j.apcatb.2018.09.025

(31) Ren, W. H.; Tan, X.; Yang, W. F.; Jia, C.; Xu, S. M.; Wang, K. X.; Smith, S. C.; Zhao, C. *Angew. Chem. Int. Ed.* **2019,** *58*, 6972. doi: 10.1002/anie.201901575

(32) Yang, J.; Qiu, Z. Y.; Zhao, C. M.; Wei, W. C.; Chen, W. X.; Li, Z. J.; Qu, Y. T.; Dong, J. C.; Luo, J.; Li, Z. Y.; *et al*. *Angew. Chem. Int. Ed*. **2018,** *57*, 14095. doi: 10.1002/anie.201808049

(33) Huang, X.; Ma, Y.; Zhi, L. *Acta Phys. -Chim. Sin.* **2022,** *38*, 2011050. [黄小雄, 马英杰, 智林杰. 物理化学学报, **2022,** *38*, 2011050.] doi: 10.3866/PKU.WHXB202011050

(34) Geng, Z.; Cao, Y.; Chen, W.; Kong, X.; Liu, Y.; Yao, T.; Lin, Y. *Appl. Catal. B* **2019,** *240*, 234. doi: 10.1016/j.apcatb.2018.08.075

(35) Pan, F.; Zhang, H.; Liu, K.; Cullen, D.; More, K.; Wang, M.; Feng, Z.; Wang, G.; Wu, G.; Li, Y. *ACS Catal.* **2018,** *8*, 3116. doi: 10.1021/acscatal.8b00398

(36) Gao, C. Y.; Liu, S. X.; Xie, L. H.; Ren, Y. H.; Cao, J. F.; Sun, C. Y. *CrystEngComm*. **2007,** *9*, 545. doi: 10.1039/B704433J